

Purity Law for Generalizable Neural TSP Solvers

Wenzhao Liu¹ Haoran Li¹ Congying Han¹ Zicheng Zhang¹ Anqi Li¹ Tiande Guo¹

Abstract

Achieving generalization in neural approaches across different scales and distributions remains a significant challenge for the Traveling Salesman Problem (TSP). A key obstacle is that neural networks often fail to learn robust principles for identifying universal patterns and deriving optimal solutions from diverse instances. In this paper, we first uncover Purity Law (PuLa), a fundamental structural principle for optimal TSP solutions, defining that edge prevalence grows exponentially with the sparsity of surrounding vertices. Statistically validated across diverse instances, PuLa reveals a consistent bias toward local sparsity in global optima. Building on this insight, we propose Purity Policy Optimization (PUPO), a novel training paradigm that explicitly aligns characteristics of neural solutions with PuLa during the solution construction process to enhance generalization. Extensive experiments demonstrate that PUPO can be seamlessly integrated with popular neural solvers, significantly enhancing their generalization performance without incurring additional computational overhead during inference.

1. Introduction

The Traveling Salesman Problem (TSP) is a fundamental combinatorial optimization (CO) problem with broad applications in operations research and computer science fields such as scheduling (Picard & Queyranne, 1978; Bagchi et al., 2006), circuit compilation (Paler et al., 2021; Duman & Or, 2004), and computational biology (Korostensky & Gonnet, 1999; Gusfield, 2019). Due to its NP-hard nature, even the most advanced exact solver (Applegate et al., 2009) could not efficiently find the optimal solution for large-scale instances within a reasonable time frame. As a result, approximate heuristic algorithms, such as LKH3 (Helsgaun, 2000; 2017), have been developed to find near-optimal solu-

¹School of Mathematical Sciences, University of Chinese Academy of Sciences, Beijing, China. Correspondence to: Congying Han <hancy@ucas.ac.cn>.

Preliminary work. Under review. Do not distribute.

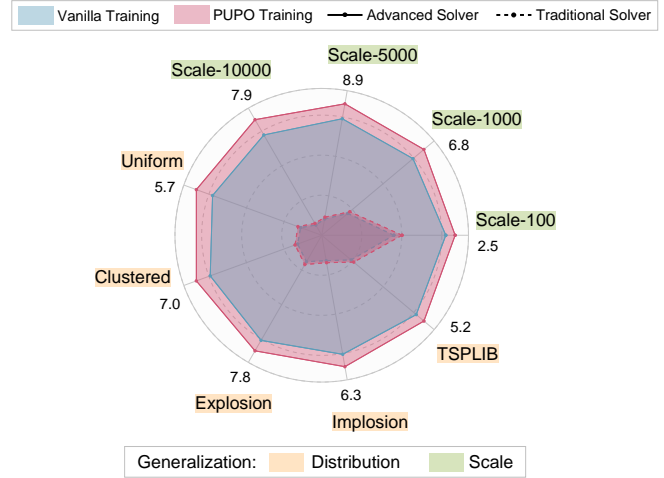


Figure 1. Generalization performance of the neural TSP solver with PUPO is significantly improved across various instance scales and distributions compared to the vanilla solver without PUPO.

tions for large instances with improved efficiency. However, these approaches still face significant computational overhead due to their iterative search processes for each instance.

Deep learning, particularly deep reinforcement learning (DRL), holds significant promise for developing fast and advanced TSP heuristics. Learning-based approaches generally fall into two categories: methods that learn to construct solutions step by step (Bello et al., 2016; Kool et al., 2018; Kwon et al., 2020; Jin et al., 2023), and methods that learn to search for better solutions iteratively (Lu et al., 2019; da Costa et al., 2021; Fu et al., 2021). Among these, neural constructive methods excel in faster inference and higher performance, enabling real-time TSP applications. However, they often struggle with generalization and exhibit limited performance on large-scale or heterogeneous instances.

The primary challenge behind this weak generalization lies in the tendency of neural models to overfit to specific patterns tied to particular training settings. To address this, some approaches have focused on simplifying the decision space, such as restricting the feasible action set (Fang et al., 2024) and employing divide-and-conquer strategies (Pan et al., 2023; Luo et al., 2023). While these methods improve performance, they inherently reduce the potential optimality of the solutions. More importantly, they lack guidance from the universal structural properties of TSP, which pre-

vents neural solvers from directly learning consistent and applicable patterns across various instances.

In this paper, we first explore generalizable structural patterns in TSP, then leverage them to guide the learning process of neural solvers. To begin with, we define edge purity order as a measure of vertex density around edges, where sparser neighborhoods yield lower purity orders. We reveal Purity Law (PuLa), a fundamental principle for TSP stating: *the proportion of different edges in the optimal solution follows a negative exponential law based on their purity orders across various instances*. This indicates that edges with lower purity orders are more prevalent in optimal solutions, with their frequency increasing exponentially as the order decreases. PuLa demonstrates its potential to capture universal structural information in two key ways. First, it is ubiquitously present in optimal solutions in various instances, underscoring *its strong connection to optimality*. Second, the parameters of its negative exponential model remain statistically invariant across varying instance scales and distributions, proving that *the sparsity-driven edge dominance law is intrinsic rather than data-specific*.

Based on the universal presence of the Purity Law, we propose **PUrity Policy Optimization (PUPO)**, a novel training framework that incorporates this generalizable structural information into the policy optimization process. PUPO guides the solution construction process by encouraging the emergence of PuLa. Specifically, it modifies the policy gradient to balance the purity metrics of solutions at different decision stages. By aligning with PuLa, PUPO helps models learn consistent patterns independent of specific instances, thereby improving their ability to generalize to different distributions and scales, without altering the underlying network architecture. Notably, PUPO can be easily integrated with a wide range of existing neural solvers. Extensive experiments show that PUPO significantly enhances the generalization ability of these solvers (shown in Fig. 1), without increasing computational overhead during inference (shown in Fig. 6). Our contributions include:

- We identify the Purity Law (PuLa) as a fundamental principle that reliably characterizes optimal solutions across various scales and distributions, offering a novel perspective for comprehending common structural patterns in TSP.
- We propose Purity Policy Optimization (PUPO), a novel training approach that explicitly encourages alignment with PuLa during the solution construction process, helping models to learn consistent patterns across different instances.
- We demonstrate through extensive experiments that PUPO can be seamlessly integrated with popular neural solvers to considerably improve their generalization, without increasing computational cost during inference.

2. Related Work

Traditional Methods. TSP solvers are typically categorized into exact, approximate, and heuristic. Concorde (Apple-gate et al., 2009), a leading exact solver, formulates TSP as a mixed integer program and uses a branch and cut algorithm (Padberg & Rinaldi, 1991) to solve it. Christofides Algorithm (Christofides, 1976), a representative approximate method, constructs solutions starting from a minimum spanning tree and finding a minimum cost perfect matching in a specific induced subgraph, achieving an approximation ratio of 1.5. LKH-3 (Helsgaun, 2017) is the SOTA heuristic method, employing local search and k-opt exchanges to iteratively improve solutions. However, achieving high-precision solutions with LKH-3 incurs significant computational costs, making it impractical for large-scale instances.

Classical Neural Solvers. With the rapid progress in deep learning, various neural approaches to combinatorial optimization have emerged. Overviews of these methods can be found in Guo et al. (2019) and Bengio et al. (2021). These approaches can generally be divided into two classes: learning to directly construct and learning to iteratively improve solutions. For constructive methods, Vinyals et al. (2015) introduces the Pointer Network, which solves TSP end-to-end utilizing Recurrent Neural Networks to encode vertex embeddings, trained via supervised learning. Transformer-based architectures in DRL further improve the encoding of node features globally and employ autoregressive decoding to generate solutions (Kool et al., 2018; Kwon et al., 2020; Bresson & Laurent, 2021). Pointerformer (Jin et al., 2023) enhances memory efficiency by adopting a reversible residual network in the encoder and a multi-pointer network in the decoder. For iterative methods, DRL-2opt (da Costa et al., 2021) trains a DRL policy to select appropriate 2-opt operators for refining solutions. GCN+MCTS (Fu et al., 2021) integrates graph decomposition and Monte Carlo Tree Search to handle large-scale instances effectively.

Advanced Solvers. Traditional Neural methods often struggle with poor generalization (Joshi et al., 2021). UTSP (Min et al., 2024) applies unsupervised learning by leveraging permutation matrix properties but fails to scale to instances larger than 2000 vertices. H-TSP (Pan et al., 2023) improves efficiency for large-scale instances by employing hierarchical DRL. LEHD (Luo et al., 2023) and GLOP (Ye et al., 2024) continuously refine solutions through divide-and-conquer strategies. PDAM (Zhang et al., 2023) and INVIT (Fang et al., 2024) simplify the decision space by restricting actions to local neighborhoods, which improves generalization. However, they inherently trade off the optimality of solutions in favor of generalization. Despite progress, no research has explored universal structural principles of TSP to guide neural learning, leaving the challenge of identifying consistent instance patterns unsolved.

3. Preliminary

In this section, we introduce the formal definition of TSP and the policy learning paradigm for TSP solutions.

3.1. Traveling Salesman Problem

In this paper, we focus on the Euclidean TSP in two-dimensional space. Given a TSP instance, let $G = (\mathcal{X}, \mathcal{E}, N)$ represents an undirected graph, where N is the number of vertices, $\mathcal{X} = \{x_i | 1 \leq i \leq N\}$ is the vertex set, and $\mathcal{E} = \{e_{ij} = (x_i, x_j) | 1 \leq i, j \leq N\}$ is the edge set. In the Euclidean TSP, G is fully connected and symmetric, with each vertex $x_i \in \mathcal{X}$ represented by a coordinate (x_i^1, x_i^2) scaled to the unit square $[0, 1]$. Each edge $e_{ij} \in \mathcal{E}$ is assigned a traversal cost $c(x_i, x_j)$, typically the Euclidean distance between the vertices x_i and x_j . A Hamiltonian cycle $\mathbf{x} = (x_{\tau_1}, x_{\tau_2}, \dots, x_{\tau_N})$ is a tour that visits each vertex exactly once. The total cost of ω is formulated as follows:

$$L(\mathbf{x}) = c(x_{\tau_N}, x_{\tau_1}) + \sum_{i=2}^N c(x_{\tau_{i-1}}, x_{\tau_i}), \quad (1)$$

The objective of solving TSP is to find the Hamiltonian cycle with the minimum total cost among all feasible cycles.

3.2. Policy Learning for the TSP

Policy learning is the dominant paradigm in DRL for solving the TSP. Given an instance \mathcal{X} , a solution $\tau = (\tau_1, \dots, \tau_N)$ is autoregressively generated through the neural policy:

$$p_\theta(\tau | \mathcal{X}) = p_\theta(\tau_1 | \mathcal{X}) \prod_{t=2}^N p_\theta(\tau_t | \tau_{1:t-1}, \mathcal{X}), \quad (2)$$

where θ are the parameters of the policy network, trained by minimizing the expected tour length:

$$\mathcal{L}(\theta | \mathcal{X}) = \mathbb{E}_{p_\theta(\tau | \mathcal{X})}[L(\tau)]. \quad (3)$$

REINFORCE (Williams, 1992) is the cornerstone of policy-based reinforcement learning methods, which computes the gradient $\nabla \mathcal{L}(\theta | \mathcal{X})$ in the context of TSP as the following:

$$\mathbb{E}_{p_\theta(\tau | \mathcal{X})} \left[(L(\tau) - b(\mathcal{X})) \sum_{t=2}^N \nabla \log p_\theta(\tau_t | \tau_{1:t-1}, \mathcal{X}) \right], \quad (4)$$

where $b(\mathcal{X})$ is a baseline for variance reduction.

4. Purity Patterns for Generalization

In this section, we first explore the structural patterns closely tied to generalization in optimal solutions. We observe that edges surrounded by sparse vertices consistently prevail across different instances. To capture this relationship, we propose the concept of *purity order*, which quantifies the density of vertices around an edge. Based on this, we uncover the Purity Law, an empirical phenomenon that reveals a universal structural principle in TSP optimal solutions.

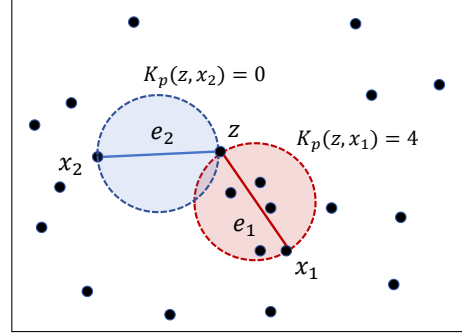


Figure 2. Example of edge purity orders with the same length.

4.1. Purity Order in Traveling Salesman Problems

We introduce the concept of purity order to formulate the vertex density around each edge.

Definition 4.1 (Purity Order). The *covering set* N_c and *purity order* K_p of an edge $e_{ij} = (x_i, x_j)$ are defined as:

$$N_c(e_{ij}) := \{x \in \mathcal{X} \mid (x_i - x)^T \cdot (x_j - x) < 0\}, \quad (5a)$$

$$K_p(e_{ij}) = K_p(x_i, x_j) := |N_c(e_{ij})|. \quad (5b)$$

Geometrically, the covering set of an edge corresponds to the vertices lying within a circle, whose diameter is defined by this edge, and the purity order is the cardinality of this set. As illustrated in Fig. 2, the purity order reflects the local density of vertices surrounding an edge. A lower purity order indicates a more sparse and “pure” configuration of vertices around the edge. For convenience, we refer to an edge with purity order k as a k -order pure edge.

Additionally, we investigate the topological properties of 0-order pure edges with the lowest redundancy (details shown in Appendix B). Specifically, we establish the *existence* of 0-order pure neighbors for any vertex, laying the groundwork for our optimization paradigm. We then prove the *connectivity* of the subgraph formed by 0-order pure edges, indicating that these edges capture global structural properties. Furthermore, we demonstrate that the polyhedron formed by the 0-order pure neighbors of any vertex is *convex*, highlighting its structural integrity and stability. This insight suggests the potential for efficient computational methods.

Intuitive Example Analysis. Purity order not only measures vertex redundancy around an edge, but also captures topological information beyond edge length. Even among edges of equal length, those with lower purity orders typically exhibit more favorable structural properties. As shown in Fig. 2, consider two edges, e_1 and e_2 , formed with vertices x_1 and x_2 from vertex z . Despite having the same length, their purity orders are 4 and 0, respectively. The edge e_1 passes through a denser region of vertices, which negatively affects the subsequent connections, making it

Table 1. Fitting results of the exponential function in Eq. (7).

	FITTING ERROR	α	β
MEAN	2.23E-05	0.92	2.63
VARIANCE	8.45E-10	1.57E-04	1.49E-02

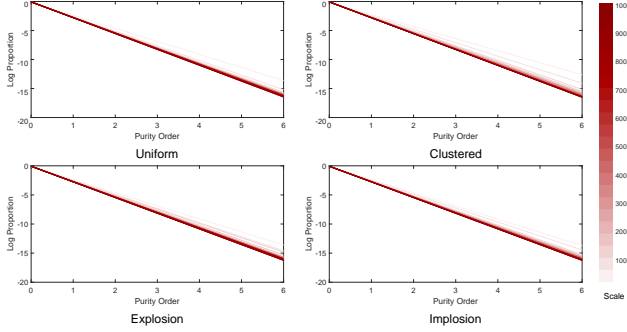


Figure 3. Purity Law curves under varying scales and distributions.

harder to form a cohesive structure. In contrast, e_2 , surrounded by sparser vertices, has minimal negative impact on the underlying connectivity of other vertices, suggesting more conducive to a well-structured solution. These observations suggest that solutions with more lower-order pure edges may have a greater potential for optimality.

4.2. Purity Law in TSP Optimal Solutions

We quantitatively investigate the distribution of purity orders in optimal solutions across various instance scales and distributions, leading to the concept of the Purity Law.

Purity Law : The distribution of edges in optimal solutions follows a *negative exponential law* based on their purity orders across various instances.

To validate the Purity Law, we conduct extensive statistical experiments on instances with varying scales and distributions. Specifically, we create datasets from 84 instance types with scales ranging from 20 to 1000, sampled from four classical distributions. The corresponding optimal solutions are computed using the LKH3 algorithm (Helsgaun, 2017). A detailed description of the dataset is provided in Append. C.

For each instance type, we calculate the purity order of every edge in the optimal solution and then statistic the proportion y of edges with a given purity order k , which is defined as:

$$y(k) = \frac{\sum_{(\tau_i^*, \tau_j^*) \in \tau^*} \mathbb{I}(K_p(\tau_i^*, \tau_j^*)=k)}{N}, \quad k \in [0, N-2], \quad (6)$$

where N is the instance scale, (τ_i^*, τ_j^*) is the edge in the optimal solution τ^* , and $\mathbb{I}(\cdot)$ is the indicator function. Next, we fit the proportions to a negative exponential function:

$$\log y(k) = -\beta k + \log \alpha, \quad (7)$$

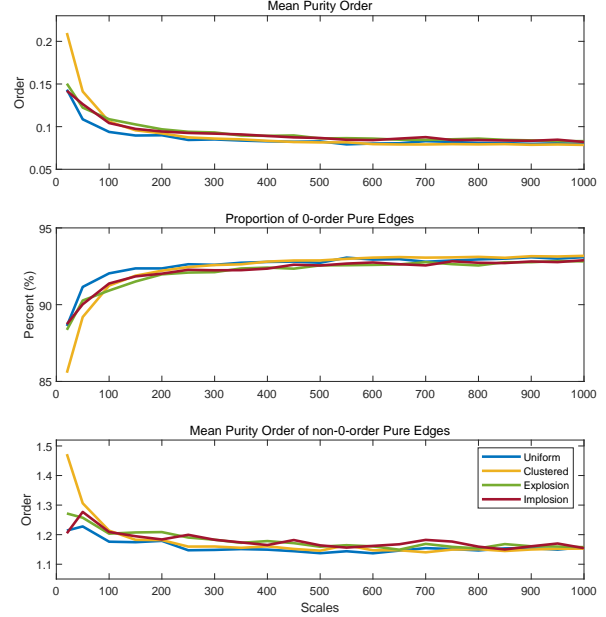


Figure 4. Mean purity order, proportion of 0-order pure edges, and average order of non-0-order pure edges for varying instance.

and present mean and variance of fitted parameters α and β , along with fitting errors, in Table 1. Further fitting results for each instance type are available in Appendix D. The remarkably low mean and variance of fitting errors underscore that the negative exponential law reliably and universally applies across different instance scales and distributions.

The negative exponential relationship reveals that purity orders of edges and their proportions in the optimal solution decrease exponentially, confirming our earlier comprehension. To better understand the decay rate, we visualize the fitted curves for different instance types in Fig. 3, where we plot the logarithm of y for clarity. As seen in Fig. 3, the coefficient α is invariant for both scales and distributions, with different curves nearly overlapping at the vertical axis intersection. The decay rate β slightly increases with instance scale, indicating that, for larger-scale instances, the proportion of each purity order decreases more rapidly.

4.3. Consistent Dominance of Lowest-order Pure Edges

The rapid decay of the negative exponential function ensures that edges with lower purity orders dominate the optimal solution, while edges with higher purity orders are seldom present. To concretely illustrate this property, we calculate the mean purity order, the proportion of 0-order pure edges, and the average order of non-0-order pure edges in optimal solutions for each instance type. The results, shown in Fig. 4, highlight the consistent dominance of 0-order pure edges.

The variations in these metrics exhibit a steady trend across different instance scales and distributions, further reinforcing the universality and stability of the Purity Law. The

mean purity order stabilizes around 0.1, indicating that the optimal tours consistently maintain a quite low level of overall purity order. Furthermore, the proportion of 0-order pure edges consistently stays around 92%, reflecting their dominant presence in optimal solutions. This proportion also aligns with the fitting parameter α . For non-0-order pure edges, which have a minimal purity order of 1, the mean purity order remains around 1.15. This suggests that, even among non-0-order pure edges, low-order pure edges are predominant, with higher-order pure edges being quite rare. Notably, all these proportions remain nearly invariant when the instance scale exceeds 300, underscoring the remarkable and dominant consistency of low-order pure edges.

5. Policy Learning Inspired by Purity Patterns

In standard neural learning for TSP, the tour length, as defined in Eq. (4), is typically the only objective for policy optimization. However, relying solely on this reward signal, neural networks often fail to capture inherent structural patterns present across different instances. Despite efforts to modify the architecture of policy networks and learning modules in previous research, the absence of guidance from generalizable structural principles, limits effective learning of universal patterns, resulting in poor generalization.

Fortunately, the widespread and stable presence of purity patterns in optimal solutions presents a promising avenue for improving generalization. Motivated by this, we introduce two key concepts—*purity availability* and *purity cost*—to characterize purity patterns for neural learning. By incorporating these into the policy training framework, we propose purity policy optimization to encourage alignment with the Purity Law, enhancing generalization in neural solvers.

5.1. Purity Availability and Purity Cost

In the Markov model of TSP, the state at time t consists of the *unvisited vertex set* \mathcal{U}_t and the *current partial solution* τ_t , which includes the visited vertex set \mathcal{V}_t . The action a_t corresponds to the vertex τ_t selected for the next visit.

Definition 5.1 (Purity Availability). The *purity availability* $\phi(\cdot)$ of the unvisited vertex set \mathcal{U}_t is defined as the average minimum available purity order, given by:

$$\phi(\mathcal{U}_t) = \frac{\sum_{x_i \in \mathcal{U}_t} \min_{x_j \in \mathcal{U}_t, j \neq i} K_p(x_i, x_j)}{|\mathcal{U}_t|}, \quad 1 \leq t \leq N. \quad (8)$$

The purity availability $\phi(\mathcal{U}_t)$ measures the potential purity order of future edges that can be formed by the unvisited vertices. We demonstrate that the ϕ is supermodular, meaning the absolute value of marginal gain in purity availability diminishes as the set \mathcal{U}_t increases. The proof is in Appendix E.

Proposition 5.2 (Supermodularity of Purity Availability). *The set function $\phi : 2^{\mathcal{X}} \rightarrow \mathbb{R}$, defined on subsets of the*

finite set \mathcal{X} , is supermodular. Specifically, for any subsets $\mathcal{A} \subseteq \mathcal{B} \subseteq \mathcal{X}$ and any vertex $x \in \mathcal{X} \setminus \mathcal{B}$, the following holds:

$$\phi(\mathcal{A} \cup \{x\}) - \phi(\mathcal{A}) \leq \phi(\mathcal{B} \cup \{x\}) - \phi(\mathcal{B}). \quad (9)$$

This indicates that, as the solution construction progresses, the absolute value of marginal improvement in purity availability becomes more significant on smaller unvisited sets.

Definition 5.3 (Purity Cost). The *purity cost* $C(\mathcal{U}_t, \tau_{t+1})$ for selecting an action τ_{t+1} at time t is defined as:

$$\begin{cases} K_p(\tau_t, \tau_{t+1}) + \phi(\mathcal{U}_{t+1}) - \phi(\mathcal{U}_t), & \text{for } t < N, \\ K_p(\tau_N, \tau_1), & \text{for } t = N. \end{cases} \quad (10)$$

The purity cost $C(\mathcal{U}_t, \tau_{t+1})$ includes both the purity order of the new edge formed by τ_t and τ_{t+1} , and the difference in purity availability before and after the action τ_{t+1} . This formulation captures both the contribution of action τ_{t+1} to the purity order of the current partial solution and its impact on the purity potential of the remaining unvisited vertices.

5.2. Policy Optimization with Purity Weightings

To improve generalization, we integrate purity costs into the policy optimization process, aligning the model with the Purity Law. This encourages the learning of structural patterns that are consistent across varying TSP instances. To assess the potential of the current state-action pair in fostering a low-purity structure for future solution construction, we introduce the purity weighting based on purity costs.

Definition 5.4 (Purity Weightings). Let δ be a discount factor. The *purity weighting* $W(\mathcal{U}_t, \tau_{t+1})$ is defined as:

$$W(\mathcal{U}_t, \tau_{t+1}) = 1 + \sum_{j=t}^N \delta^{j-t} C(\mathcal{U}_j, \tau_{j+1}). \quad (11)$$

Building on this characterization, we propose the *purity policy gradient* $\nabla \mathcal{L}_{\text{PUPPO}}(\theta|\mathcal{X})$ as the following formulation:

$$\mathbb{E}_{p_\theta(\tau|\mathcal{X})} \left[L(\tau) \sum_{t=2}^N W_t \nabla \log p_\theta(\tau_t | \tau_{1:t-1}, \mathcal{X}) \right], \quad (12)$$

where W_{t+1} denotes the shorthand for $W(\mathcal{U}_t, \tau_{t+1})$.

The complete description of the Purity Policy Optimization (PUPPO) framework is presented in Appendix F. PUPPO establishes upon the REINFORCE algorithm with a baseline, incorporating generalizable purity patterns into the modified policy gradient. At each stage of the solution construction, PUPPO employs a discounted purity cost that reflects the purity potential of both the current partial solution and the unvisited vertex set, encouraging the model to favor actions with lower purity orders during training. This

Table 2. The experimental results of average gap (%) on the randomly generated dataset with different distributions and scales after training each model using both the vanilla and PUPO methods, where - means out of memory, bold formatting represents superior results. It can be observed that PUPO training enhances the performance of six models across nearly all instance type.

Distribution	Scale	AM-50		AM-100		PF-50		PF-100		INViT-50		INViT-100	
		Vanilla	PUPO	Vanilla	PUPO	Vanilla	PUPO	Vanilla	PUPO	Vanilla	PUPO	Vanilla	PUPO
Uniform	100	5.21	5.35	5.07	4.61	4.16	4.31	3.64	3.39	2.14	2.17	2.61	2.35
	1000	35.51	34.01	31.23	30.16	41.00	39.10	30.57	29.93	7.27	7.17	7.41	6.26
	5000	67.99	65.12	80.64	68.42	113.55	104.09	80.59	77.53	9.41	9.09	9.39	8.05
	10000	-	-	-	-	-	-	-	-	7.89	7.63	7.51	6.25
Clustered	100	7.75	8.03	7.66	6.07	7.67	7.71	7.24	6.90	2.90	2.86	3.59	3.22
	1000	41.14	39.82	37.99	33.84	51.04	49.58	47.50	44.11	8.44	8.00	8.37	7.20
	5000	77.78	75.93	76.37	70.03	137.51	131.61	137.15	121.79	9.90	9.45	9.65	8.55
	10000	-	-	-	-	-	-	-	-	10.85	10.09	10.47	9.11
Explosion	100	5.01	5.18	5.04	4.71	4.98	5.12	4.74	4.65	2.15	2.11	2.70	2.41
	1000	35.57	35.07	32.97	30.20	46.04	45.34	41.60	37.73	9.61	9.18	9.61	8.77
	5000	71.95	66.66	74.55	66.33	133.99	129.02	120.96	110.16	12.44	11.65	11.45	10.41
	10000	-	-	-	-	-	-	-	-	11.22	10.61	10.96	9.62
Implosion	100	5.02	5.17	5.12	4.64	4.71	4.91	4.49	4.35	2.44	2.38	2.77	2.62
	1000	37.38	37.12	32.44	30.94	46.54	44.83	36.11	34.47	7.56	7.50	7.81	6.90
	5000	78.57	74.05	72.87	66.58	151.37	138.71	120.67	103.74	9.20	8.86	9.44	8.96
	10000	-	-	-	-	-	-	-	-	8.36	7.68	8.27	6.78

approach helps the model to learn consistent, cross-instance patterns that align with the purity law, thereby enhancing its generalization capability. Notably, PUPO is flexible and can be integrated with various popular constructive neural solvers, without any alterations to the network architecture.

6. Numerical Experiments

To validate the effect of PUPO on enhancing generalization, we compare the performance of both vanilla policy optimization and purity policy optimization across several state-of-the-art constructive neural solvers. Additionally, we conduct a comprehensive evaluation of generalization performance and purity metrics on well-known public datasets.

6.1. Experimental Setups

Dataset. To ensure the adequacy of the experiments, we validate the model’s performance on two categories of datasets. The randomly generated dataset used in this paper is the same as that in INViT (Fang et al., 2024), which is widely adopted to testify existing DRL approach. It contains 16 subsets and corresponding (near-)optimal solutions for TSP, including 4 distributions (uniform, clustered, explosion, and implosion) and 4 scales (100, 1000, 5000 and 10000). The real-world dataset we used is TSPLIB, a well-known TSP library (Reinelt, 1991) that contains 100 instances with various nodes distributions and their optimal solutions. These instances come from practical applications with scale ranging from 14 to 85,900. In our experiment, we consider all

instances with no more than 10000 nodes.

Comparison Methods. Although PUPO can be integrated with any DRL-based neural constructive model, we select three representative SOTA methods with high recognition for our experiments: (1) AM (Kool et al., 2018), a high-performance neural constructive approach widely regarded as a benchmark, which first incorporates the transformer to solve the TSP; (2) PF (Jin et al., 2023), a neural constructive approach that designs reversible residual networks and multi-pointer networks to efficiently limit memory consumption; (3) INViT (Fang et al., 2024), the latest method that enhances generalization ability by constraining the action space and employing multi-view encoding. For each method, we conduct training on scales of 50 and 100, resulting in a total of 6 comparison configurations: AM-50, AM-100, PF-50, PF-100, INViT-50, and INViT-100.

Evaluation Metrics. We report three widely adopted performance metrics to evaluate the generalizability of each comparison method, including the average length of solutions, the average gap to the optimal solutions, and the average solving time. The gap characterizes the relative difference between the output solution of neural models and the optimal solution, which is calculated as the following:

$$gap = \frac{L(\tau^{model}) - L(\tau^{opt})}{L(\tau^{opt})} \times 100\% \quad (13)$$

We also present three metrics to reflect the ability of the model to perceive purity information: the average purity order (APO (all) for short), the proportion of 0-order pure



Figure 5. Heatmap of relatively improved accuracy after PUPO training of each model on the randomly generated dataset. From the figure, it can be observed that PUPO achieve outstanding improvement of generalizability on most instance types.

edges (Prop-0 (%) for short), and the average order of non-0-order pure edges (APO (non-0) for short) for each solution.

Experimental Settings. All the numerical experiments are implemented on an NVIDIA GeForce RTX 3090 GPU with 24 GB of memory, paired with a 12th Gen Intel(R) Core(TM) i9-12900 CPU. We train each model using the vanilla REINFORCE algorithm and PUPO, respectively. In each training paradigm, we use the original network architectures provided in the source code, *without any modifications to modules*. Additionally, all training procedures and hyperparameter remain completely consistent with the original source code, except for the learning rate. Due to the difference in the policy gradient between PUPO and the original method, we adjust the learning rates for the six models during PUPO. Specifically, the learning rates are set to 0.0001, 0.00015, 0.0001, 0.00017, 0.00011, 0.00012 for AM-50, AM-100, Pointerformer-50, Pointerformer-100, INVIT-50, and INVIT-100, respectively. All models are trained on instances randomly sampled from a uniform distribution.

6.2. Generalization Performance Analysis

Performance on Randomly Generated Dataset. Table 2 presents the performance of six models on a randomly generated dataset, trained using both the vanilla and PUPO methods. The experimental results for tour length and solving time are provided in Appendix G. It can be observed that PUPO training enhances the performance of six models across nearly all instance types. In particular, AM-100, PF-100 and INVIT-100 demonstrate superior performance across all distributions and scales compared to those trained with the vanilla. Notably, the PUPO-trained INVIT-100 accomplishes a gap of 6.78% on Implosion-10000, whereas the Vanilla-trained model can only reach a gap of 8.27%.

To better illustrate the improvement in generalizability with

Table 3. Performance of average gap (%) on TSPLIB after training each model using both the vanilla and PUPO methods. Blue highlights the decrease in the gap, while red indicates its increase. From the table, it can be observed that PUPO can also enhance the generalization ability on real-world dataset.

		1 ~ 100	101 ~ 1000	1001 ~ 5000
AM-50	Vanilla	5.82	17.39	48.41
	PUPO	5.17 ↓0.65	16.14 ↓1.25	46.48 ↓1.93
AM-100	Vanilla	4.98	14.12	43.33
	PUPO	4.48 ↓0.50	12.17 ↓1.95	40.46 ↓2.97
PF-50	Vanilla	7.42	25.96	75.57
	PUPO	8.37 ↑0.95	24.77 ↓1.19	72.58 ↓2.99
PF-100	Vanilla	7.82	23.37	66.05
	PUPO	7.16 ↓0.66	22.68 ↓0.69	60.86 ↓5.19
INVIT-50	Vanilla	1.71	4.97	9.65
	PUPO	2.02 ↑0.31	4.67 ↓0.30	8.49 ↓1.16
INVIT-100	Vanilla	2.43	5.60	9.32
	PUPO	2.16 ↓0.27	4.97 ↓0.63	8.68 ↓0.64

PUPO, Figure 5 presents a heatmap of the average relative performance improvement across various scales and distributions. Combining PUPO with larger training scales leads to more significant gains. Specifically, models trained at scale 100 achieved approximately 10% better performance, while those trained at the scale of 50 saw only a 3% gain.

From the perspective of test scale, PUPO training significantly improves model generalization performance on larger instances. For example, INVIT-100 achieves a 15.01% enhancement on the scale 10000, and AM-100 shows a 10.77% gain on the scale of 5000. On scales closer to the training scale, diverse phenomena can be observed. AM-100 accomplishes an 11.42% uplift on the scale of 100, while AM-50 and PF-50 experience negative performance changes on the same scale. This suggests that for models with poor expressive ability, PUPO may involve in a trade-off, sacrificing accuracy on smaller-scale instances while learning patterns more suited to larger scales. This trade-off is linked to the implicit regularization feature of PUPO, which is discussed in the subsequent part. From a distributional perspective, PUPO leads to positive average relative improvements across all distributions, indicating an enhancement in generalizability with respect to distributions.

Performance on Real-world Dataset. Table 3 presents the performance on TSPLIB, further demonstrating that PUPO enhances the generalization ability on real-world data.

Furthermore, it is evident that the integration of PUPO with competitive models yields significant improvements in generalization. As a SOTA constructive neural architecture, INVIT shows notable performance boosts after PUPO training, regardless of the training scale. Although PUPO also enhanced the generalizability of AM and PF, their global perception and decision modules remain vulnerable, resulting in larger performance gaps as the scale increases. This observation abstracts us to focus on developing network architectures that incorporate PuLa in future work.

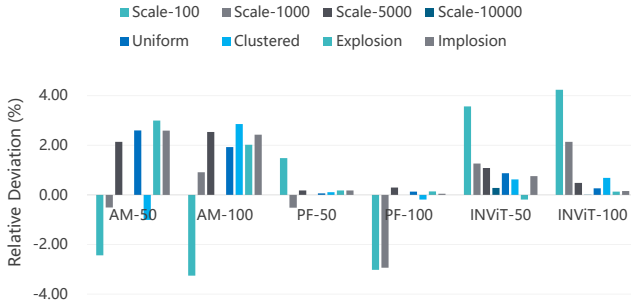


Figure 6. The bar chart of relative deviations (%) in solving time between Vanilla- and PUPU-trained models, where positive values indicate that PUPU-trained models hold shorter solving times. From the figure, it can be observed that there is no significant difference between Vanilla- and PUPU-trained model.

6.3. Computational Efficiency Analysis

Figure 6 illustrates the relative deviations in solving time between Vanilla-trained and PUPU-trained models, where positive values indicate that PUPU-trained models hold shorter solving times. Following the figure, the relative deviations are within 5% across all instance types, suggesting negligible differences between the two, even the PUPU-trained models tend to solve faster in most cases. Since PUPU only provides guidance during the training phase, it does not introduce additional time overhead during the inference phase. Due to the tensorizable computation of PUPU, the training time does not increase significantly. A detailed comparison of training times can be found in Appendix G.

6.4. Learning Mechanisms Analysis

Purity Perception. To further explore the role of PUPU during the training process, Table 4 presents three metrics that evaluate the purity of tours obtained by INVIT-100. Numerical results of purity metrics for all models are available in Appendix G. The table demonstrates that PUPU-trained models consistently generate solutions with more outstanding purity. Compared to vanilla training, PUPU enhances the Prop-0 metric across all types, and it lead to a reduction in the two kinds of APO metric across nearly all types. Notably, the largest average improvement in Prop-0 occurs at the scale of 10,000, with a 1.1% increase, which also corresponds to the scale where INVIT-100 achieves its most promoted generalization performance. These results suggest that PUPU facilitates the emergence of PuLa during training, leading to enhanced model generalization.

Implicit Regularization. Furthermore, we calculate the sum of the Frobenius norm of the parameter matrices for each model after different training, as presented in Table 5. It can be observed that PUPU training reduces the sum of the parameter norms, acting as an implicit regularization mechanism. In contrast, we also perform explicit regulariza-

Table 4. The experimental results of Vanilla- and PUPU-trained model on three purity evaluation metrics, where bold formatting represents superior results. From the table, it can be observed that PUPU enhances the ability of purity perception.

	Prop-0 (%)		APO (all)		APO (non-0)	
	Vanilla	PUPU	Vanilla	PUPU	Vanilla	PUPU
100	80.02	80.53	0.13	0.12	1.16	1.12
1000	85.46	86.48	0.23	0.19	1.81	1.66
5000	43.36	43.95	0.31	0.24	2.52	2.10
10000	87.17	88.27	0.54	0.55	4.28	4.86
Uniform	74.36	75.23	0.17	0.14	1.44	1.33
Clustered	73.82	74.65	0.34	0.33	2.76	3.02
Explosion	73.91	74.71	0.48	0.42	3.85	3.64
Implosion	73.91	74.64	0.21	0.20	1.73	1.74

Table 5. The sum of Frobenius norm of the parameter matrices for each model after different training, where bold formatting represents superior results. It can be observed that PUPU reduces the sum of the parameter norms, acting as implicit regularization.

	AM-50	AM-100	INVIT-50	INVIT-100
Vanilla	63.07	64.07	79.21	79.10
PUPU	60.22	62.82	79.15	78.89

tion training by directly incorporating the sum of the norms into the reward function, but it does not result in improved generalizability. This suggests that PUPU effectively mitigates overfitting on the specific training set, encouraging the model to learn more generalizable structural patterns.

7. Conclusion

In this paper, we reveal Purity Law (PuLa), a fundamental structural principle for optimal TSP solutions, which defines that edge prevalence grows exponentially with the sparsity of surrounding vertices. And we propose Purity Policy Optimization (PUPU) to explicitly promote alignment with PuLa during the solution construction process. Extensive experiments demonstrate that PUPU can be seamlessly integrated with popular neural solvers, significantly enhancing their generalization performance without incurring additional computational overhead during inference. PuLa provides a novel perspective on TSP, revealing a systematic bias toward local sparsity in global optima validated across diverse instances statistically. In future work, on one hand, we aim to extend PuLa to general routing problems and provide a more profound theoretical explanation of its mechanism. On the other hand, the implicit regularization properties induced by PUPU and other learning phenomenon characterized in the experiment are also worthy of further study. What’s more, we plan to explore more effective training methods for leveraging PuLa, and design network architectures that integrate PuLa to promote the perception to it, thereby achieving greater generalizability.

Impact Statement

Due to the NP-hard nature and wide application range, TSP is fundamental in combinatorial optimization problems. However, the complex structure of problem makes it challenging to conclude the general properties of TSP. Compared to traditional time-consuming methods, neural approaches are considered to possess the potential for fast and high-quality solutions. But existing learning-based methods suffer from poor generalizability. Therefore, it is meaningful to uncover the universal and stable patterns present in optimal TSP solutions and apply them to guide the learning process of models, thereby improving their generalizability without additional computational overhead. In addition to improving the related machine learning fields, the contribution can be further extended to industries like logistics, circuit compilation or computational biology.

References

- Applegate, D. L., Bixby, R. E., Chvátal, V., Cook, W., Espinoza, D. G., Goycoolea, M., and Helsgaun, K. Certification of an optimal tsp tour through 85,900 cities. *Operations Research Letters*, 37(1):11–15, 2009. ISSN 0167-6377. doi: <https://doi.org/10.1016/j.orl.2008.09.006>. URL <https://www.sciencedirect.com/science/article/pii/S0167637708001132>.
- Bagchi, T. P., Gupta, J. N., and Sriskandarajah, C. A review of tsp based approaches for flowshop scheduling. *European Journal of Operational Research*, 169(3):816–854, 2006.
- Bello, I., Pham, H., Le, Q. V., Norouzi, M., and Bengio, S. Neural combinatorial optimization with reinforcement learning. *arXiv preprint arXiv:1611.09940*, 2016.
- Bengio, Y., Lodi, A., and Prouvost, A. Machine learning for combinatorial optimization: a methodological tour d’horizon. *European Journal of Operational Research*, 290(2):405–421, 2021.
- Bresson, X. and Laurent, T. The transformer network for the traveling salesman problem. *arXiv preprint arXiv:2103.03012*, 2021.
- Christofides, N. Worst-case analysis of a new heuristic for the travelling salesman problem. *Operations Research Forum*, 3, 1976. URL <https://api.semanticscholar.org/CorpusID:123194397>.
- da Costa, P., Rhuggenaath, J., Zhang, Y., Akcay, A., and Kaymak, U. Learning 2-opt heuristics for routing problems via deep reinforcement learning. *SN Computer Science*, 2, 09 2021. doi: 10.1007/s42979-021-00779-2.
- Duman, E. and Or, I. Precedence constrained tsp arising in printed circuit board assembly. *International Journal of Production Research*, 42(1):67–78, 2004.
- Fang, H., Song, Z., Weng, P., and Ban, Y. INViT: A generalizable routing problem solver with invariant nested view transformer. In Salakhutdinov, R., Kolter, Z., Heller, K., Weller, A., Oliver, N., Scarlett, J., and Berkenkamp, F. (eds.), *Proceedings of the 41st International Conference on Machine Learning*, volume 235 of *Proceedings of Machine Learning Research*, pp. 12973–12992. PMLR, 21–27 Jul 2024. URL <https://proceedings.mlr.press/v235/fang24c.html>.
- Fu, Z.-H., Qiu, K.-B., and Zha, H. Generalize a small pre-trained model to arbitrarily large tsp instances. In *Proceedings of the AAAI conference on artificial intelligence*, volume 35, pp. 7474–7482, 2021.
- Guo, T., Han, C., Tang, S., and Ding, M. Solving combinatorial problems with machine learning methods. *Nonlinear Combinatorial Optimization*, pp. 207–229, 2019.
- Gusfield, D. Integer linear programming in computational biology: Overview of ilp, and new results for traveling salesman problems in biology. *Bioinformatics and Phylogenetics: Seminal Contributions of Bernard Moret*, pp. 373–404, 2019.
- Helsgaun, K. An effective implementation of the lin-kernighan traveling salesman heuristic. *European journal of operational research*, 126(1):106–130, 2000.
- Helsgaun, K. An extension of the lin-kernighan-helsgaun tsp solver for constrained traveling salesman and vehicle routing problems. *Roskilde: Roskilde University*, 12: 966–980, 2017.
- Jin, Y., Ding, Y., Pan, X., He, K., Zhao, L., Qin, T., Song, L., and Bian, J. Pointerformer: Deep reinforced multi-pointer transformer for the traveling salesman problem. In *Proceedings of the AAAI Conference on Artificial Intelligence*, volume 37, pp. 8132–8140, 2023.
- Joshi, C. K., Cappart, Q., Rousseau, L.-M., and Laurent, T. Learning tsp requires rethinking generalization. In *International Conference on Principles and Practice of Constraint Programming*, 2021.
- Kool, W., Van Hoof, H., and Welling, M. Attention, learn to solve routing problems! *arXiv preprint arXiv:1803.08475*, 2018.
- Korostensky, C. and Gonnet, G. Near optimal multiple sequence alignments using a traveling salesman problem approach. In *6th International Symposium on String Processing and Information Retrieval. 5th International Workshop on Groupware (Cat. No. PR00268)*, pp. 105–114, 1999. doi: 10.1109/SPIRE.1999.796584.

- Kwon, Y.-D., Choo, J., Kim, B., Yoon, I., Gwon, Y., and Min, S. Pomo: Policy optimization with multiple optima for reinforcement learning. *Advances in Neural Information Processing Systems*, 33:21188–21198, 2020.
- Langley, P. Crafting papers on machine learning. In Langley, P. (ed.), *Proceedings of the 17th International Conference on Machine Learning (ICML 2000)*, pp. 1207–1216, Stanford, CA, 2000. Morgan Kaufmann.
- Lu, H., Zhang, X., and Yang, S. A learning-based iterative method for solving vehicle routing problems. In *International conference on learning representations*, 2019.
- Luo, F., Lin, X., Liu, F., Zhang, Q., and Wang, Z. Neural combinatorial optimization with heavy decoder: Toward large scale generalization. In Oh, A., Naumann, T., Globerson, A., Saenko, K., Hardt, M., and Levine, S. (eds.), *Advances in Neural Information Processing Systems*, volume 36, pp. 8845–8864. Curran Associates, Inc., 2023. URL https://proceedings.neurips.cc/paper_files/paper/2023/file/1c10d0c087c14689628124bbc8fa69f6-Paper-Conference.pdf.
- Min, Y., Bai, Y., and Gomes, C. P. Unsupervised learning for solving the travelling salesman problem. *Advances in Neural Information Processing Systems*, 36, 2024.
- Padberg, M. and Rinaldi, G. A branch-and-cut algorithm for the resolution of large-scale symmetric traveling salesman problems. *SIAM review*, 33(1):60–100, 1991.
- Paler, A., Zulehner, A., and Wille, R. Nisq circuit compilation is the travelling salesman problem on a torus. *Quantum Science and Technology*, 6(2):025016, mar 2021. doi: 10.1088/2058-9565/abe665. URL <https://dx.doi.org/10.1088/2058-9565/abe665>.
- Pan, X., Jin, Y., Ding, Y., Feng, M., Zhao, L., Song, L., and Bian, J. H-tsp: Hierarchically solving the large-scale traveling salesman problem. *Proceedings of the AAAI Conference on Artificial Intelligence*, 37(8):9345–9353, Jun. 2023. doi: 10.1609/aaai.v37i8.26120. URL <https://ojs.aaai.org/index.php/AAAI/article/view/26120>.
- Picard, J.-C. and Queyranne, M. The time-dependent traveling salesman problem and its application to the tardiness problem in one-machine scheduling. *Operations research*, 26(1):86–110, 1978.
- Reinelt, G. TspLib - a traveling salesman problem library. OR Software, 1991. Available at <http://www.iwr.uni-heidelberg.de/iwr/comopt/software/TSPLIB95/>.
- Vinyals, O., Fortunato, M., and Jaitly, N. Pointer networks. *Advances in neural information processing systems*, 28, 2015.
- Williams, R. J. Simple statistical gradient-following algorithms for connectionist reinforcement learning. *Machine learning*, 8:229–256, 1992.
- Ye, H., Wang, J., Liang, H., Cao, Z., Li, Y., and Li, F. Glop: Learning global partition and local construction for solving large-scale routing problems in real-time. *Proceedings of the AAAI Conference on Artificial Intelligence*, 38(18):20284–20292, Mar. 2024. doi: 10.1609/aaai.v38i18.30009. URL <https://ojs.aaai.org/index.php/AAAI/article/view/30009>.
- Zhang, D., Xiao, Z., Wang, Y., Song, M., and Chen, G. Neural tsp solver with progressive distillation. *Proceedings of the AAAI Conference on Artificial Intelligence*, 37(10):12147–12154, Jun. 2023. doi: 10.1609/aaai.v37i10.26432. URL <https://ojs.aaai.org/index.php/AAAI/article/view/26432>.

A. Details of the Radar Chart Construction

We select AM-100 and INViT-100 to represent the traditional and advanced solvers, respectively. The average gaps for each solver are computed across four scales and five distributions, which are listed in Table 6. The reciprocal of the gap is then taken, and the values are normalized to the maximum value within each dimension. These derived metrics are used to plot the radar chart.

Table 6. The Experimental results used to plot the radar chart.

		Scale-100	Scale-1000	Scale-5000	Scale-10000	Uniform	Clustered	Explosion	Implosion	TSPLIB
AM-100	Vanilla	5.57	29.75	69.55	100.00	38.98	40.67	37.52	36.81	20.81
	PUPO	4.90	27.46	62.36	86.00	34.40	36.65	33.74	34.05	19.03
INViT-100	Vanilla	2.82	7.76	8.85	9.30	6.73	8.02	8.68	7.07	5.78
	PUPO	2.55	6.82	7.73	7.94	5.73	7.02	7.80	6.31	5.27

B. Topological Properties of 0-order Pure Edges

As the class of edges with the lowest degree of redundancy, 0-order pure edges are demonstrated by the following propositions to possess a series of favorable topological properties.

Proposition B.1. *Given an instance \mathcal{X} , for any vertex $x \in \mathcal{X}$, there exists at least one vertex that can form a 0-order pure edge with x .*

Proof. We prove the proposition by contradiction.

Assume that for any $x \in \mathcal{X}$, we choose

$$y(x) := \arg \min \|x - y\|^2.$$

Since no vertex can form a 0-order pure edge with x , we have that

$$K_p(x, y(x)) > 0, \quad \forall x \in \mathcal{X}.$$

Therefore, there must exist a point $z(x)$ such that

$$(x - z(x))^T (y(x) - z(x)) < 0.$$

Then we can derive that

$$\begin{aligned} & \|x - y(x)\|^2 \\ &= \|x - z(x) + z(x) - y(x)\|^2 \\ &= \|x - z(x)\|^2 + \|z(x) - y(x)\|^2 - 2(x - z(x))^T (y(x) - z(x)) \\ &\geq \|x - z(x)\|^2 + \|z(x) - y(x)\|^2 \\ &\geq \|x - z(x)\|^2, \end{aligned}$$

which means that the distance between $z(x)$ and x is smaller than the distance between $y(x)$ and x . Therefore, it contradicts the assumption that $y(x)$ is the nearest neighbor of x . \square

Proposition B.2. *Given an instance \mathcal{X} , the subgraph $G_0 = (\mathcal{X}, \mathcal{E}_0)$ is connected, where \mathcal{E}_0 is the edge set of all 0-order pure edges.*

Proof. We prove the proposition by contradiction.

Suppose the subgraph G_0 is not connected. Without loss of generality, assume that G_0 has two connected components, denoted as F_1 and F_2 . Let $f_1 \in F_1$ and $f_2 \in F_2$ be such that

$$\text{dist}(f_1, f_2) = \text{dist}(F_1, F_2) = \min_{a \in F_1} \min_{b \in F_2} \text{dist}(a, b).$$

Since $e_{f_1 f_2} \notin G_0$, we have that

$$K_p(f_1, f_2) > 0.$$

Therefore, there must exist a point f_3 such that the following inequality holds:

$$(f_1 - f_3)^T (f_2 - f_3) < 0,$$

which means that the distance between f_3 and f_1 is smaller than the distance between f_2 and f_1 . Regardless of whether $f_3 \in F_1$ or $f_3 \in F_2$, this leads to a contradiction with the assumption that the distance between f_1 and f_2 is the shortest distance between F_1 and F_2 . □

Proposition B.3. *Given an instance \mathcal{X} , for any vertex $x \in \mathcal{X}$, the polyhedron formed by its 0-order pure neighbors D_0^x is convex.*

Proof. Consider any three adjacent 0-order pure neighbors A , B , and C of point X . We have that

$$\angle ABC = \angle ABX + \angle XBC.$$

Since A and C are 0-order pure neighbors of X , it follows that

$$\angle ABX, \angle XBC < \frac{\pi}{2},$$

and thus $\angle ABC < \pi$.

Due to the arbitrariness of A , B , and C , the polyhedron formed by its 0-order pure neighbors D_0^x is convex. □

Proposition B.1 establishes the existence of 0-order pure neighbors for any point, providing a foundation for subsequent analysis. While proposition B.2 demonstrates that the subgraph formed by 0-order pure edges possesses overall graph structural properties. And proposition B.3 describes the intrinsic topological features of the 0-order neighbor set for any given point. The three propositions above characterize the mathematical properties of purity order theoretically.

C. Dataset Description

To construct the dataset in statistical experiments, we first generate 21 different scales within the range of 20 to 1000, with intervals of 50 except 20. For each scale, we consider four widely recognized classical distributions, which is uniform, cluster, explosion and implosion, resulting in 84 different instance types totally. For instance types with scales under 500, 256 instances are randomly sampled to form the dataset, while for those with sizes of 500 or above, the number of instances is reduced to 128, which is due to the fact that optimal solutions of large-scale instances require an excessive amount of time. The optimal solutions for all instances are solved by LKH-3 (Helsgaun, 2000; 2017), which is the SOTA heuristic capable of producing optimal solutions even for large-scale instances.

D. Detailed Fitting Result

The detailed values of the fitting error, α and β for each instance type are listed in Table 7. According to the table, the low mean and variance of the fitting errors demonstrate the reliability and universality of the fitting results across different instance scales and distributions.

E. Proof of the supermodularity of Purity Availability ϕ

Proposition E.1. *The set function $\phi : 2^X \rightarrow \mathbb{R}$ defined on the subsets of the finite set X is supermodular, that is, for any subset $A \subseteq B \subseteq X$ and any $x \in X \setminus B$, the following inequality holds:*

$$\phi(A \cup \{x\}) - \phi(A) \leq \phi(B \cup \{x\}) - \phi(B).$$

Table 7. The fitting errors, coefficients α and β in Sec. 4.2

	Fitting Error				α				β			
	Uniform	Clustered	Explosion	Implosion	Uniform	Clustered	Explosion	Implosion	Uniform	Clustered	Explosion	Implosion
20	6.58E-05	2.45E-04	1.01E-04	5.71E-05	0.8860	0.8554	0.8835	0.8872	2.2514	2.0800	2.2483	2.2630
50	5.42E-05	7.90E-05	3.96E-05	5.05E-05	0.9115	0.8919	0.9027	0.9002	2.5166	2.3295	2.4152	2.3923
100	2.41E-05	3.75E-05	1.85E-05	3.61E-05	0.9204	0.9124	0.9091	0.9137	2.5974	2.5133	2.4567	2.5286
150	2.54E-05	2.57E-05	2.96E-05	1.78E-05	0.9236	0.9188	0.9150	0.9184	2.6410	2.5782	2.5412	2.5681
200	2.18E-05	2.20E-05	2.62E-05	1.63E-05	0.9236	0.9221	0.9197	0.9202	2.6384	2.6192	2.6002	2.5887
250	1.18E-05	1.35E-05	2.38E-05	2.42E-05	0.9263	0.9245	0.9209	0.9227	2.6568	2.6366	2.6066	2.6337
300	1.26E-05	1.49E-05	2.06E-05	2.08E-05	0.9259	0.9258	0.9211	0.9224	2.6535	2.6578	2.6057	2.6201
350	1.39E-05	1.40E-05	1.61E-05	1.71E-05	0.9273	0.9263	0.9236	0.9224	2.6762	2.6621	2.6318	2.6166
400	1.33E-05	1.54E-05	1.80E-05	1.05E-05	0.9278	0.9280	0.9241	0.9235	2.6814	2.6918	2.6430	2.6206
450	1.04E-05	1.12E-05	1.61E-05	1.52E-05	0.9280	0.9288	0.9234	0.9260	2.6805	2.6947	2.6289	2.6633
500	8.38E-06	1.15E-05	1.18E-05	1.28E-05	0.9273	0.9288	0.9256	0.9255	2.6634	2.6936	2.6515	2.6536
550	1.04E-05	1.49E-05	1.94E-05	1.31E-05	0.9306	0.9298	0.9257	0.9267	2.7190	2.7186	2.6615	2.6673
600	7.55E-06	1.08E-05	1.48E-05	1.26E-05	0.9294	0.9306	0.9259	0.9275	2.6931	2.7207	2.6591	2.6803
650	1.13E-05	1.37E-05	9.63E-06	1.79E-05	0.9297	0.9310	0.9262	0.9263	2.7058	2.7293	2.6535	2.6689
700	1.34E-05	1.02E-05	1.40E-05	1.77E-05	0.9280	0.9306	0.9277	0.9256	2.6856	2.7175	2.6877	2.6563
750	1.22E-05	1.19E-05	1.50E-05	1.26E-05	0.9287	0.9308	0.9264	0.9282	2.6959	2.7251	2.6658	2.6930
800	1.22E-05	1.29E-05	9.97E-06	1.19E-05	0.9294	0.9311	0.9255	0.9273	2.7040	2.7323	2.6459	2.6750
850	1.30E-05	1.12E-05	1.80E-05	1.33E-05	0.9300	0.9305	0.9276	0.9271	2.7151	2.7184	2.6909	2.6707
900	1.33E-05	1.03E-05	1.08E-05	1.46E-05	0.9309	0.9316	0.9276	0.9281	2.7296	2.7357	2.6790	2.6906
950	1.33E-05	1.38E-05	1.44E-05	1.41E-05	0.9299	0.9314	0.9284	0.9277	2.7132	2.7376	2.6951	2.6855
1000	1.51E-05	1.21E-05	1.26E-05	1.24E-05	0.9310	0.9318	0.9282	0.9289	2.7340	2.7413	2.6890	2.6978

Proof. Given subsets $U \subseteq X$ and any $v_1, v_2 \in X \setminus U$, we prove the equivalent definition of submodular functions:

$$\phi(U \cup \{v_1\}) + \phi(U \cup \{v_2\}) \leq \phi(U \cup \{v_1, v_2\}) + \phi(U). \quad (14)$$

First, we have

$$\begin{aligned} \phi(U) &= \frac{\sum_{x_i \in U} \min_{\substack{x_j \in U \\ j \neq i}} K_p(x_i, x_j)}{|U|}. \\ \phi(U \cup \{v_1\}) &= \frac{\sum_{x_i \in U} \min_{\substack{x_j \in U \cup \{v_1\} \\ j \neq i}} K_p(x_i, x_j) + \min_{x_j \in U} K_p(v_1, x_j)}{|U| + 1} \\ \phi(U \cup \{v_2\}) &= \frac{\sum_{x_i \in U} \min_{\substack{x_j \in U \cup \{v_2\} \\ j \neq i}} K_p(x_i, x_j) + \min_{x_j \in U} K_p(v_2, x_j)}{|U| + 1} \\ \phi(U \cup \{v_1, v_2\}) &= \frac{\sum_{x_i \in U} \min_{\substack{x_j \in U \cup \{v_1, v_2\} \\ j \neq i}} K_p(x_i, x_j) + \min_{x_j \in U \cup \{v_2\}} K_p(v_1, x_j) + \min_{x_j \in U \cup \{v_1\}} K_p(v_2, x_j)}{|U| + 2}. \end{aligned}$$

By the following relations, we partition U into three parts, denoted as U_0, U_1, U_2 , respectively.

$$U_0 = \{x_i \mid \arg \min_y K_p(x_i, y) \in U\}$$

$$U_1 = \{x_i \mid \arg \min_y K_p(x_i, y) = v_1\}$$

$$U_2 = \{x_i \mid \arg \min_y K_p(x_i, y) = v_2\}$$

Then, we prove that the following expression is non-positive from three parts.

$$(\phi(U \cup \{v_1\}) + \phi(U \cup \{v_2\})) - (\phi(U \cup \{v_1, v_2\}) + \phi(U)).$$

Part 1

$$\begin{aligned} & \sum_{x_i \in U_0} \min_{x_j \in U} K_p(x_i, x_j) \left[\frac{2}{|U|+1} - \left(\frac{1}{|U|} + \frac{1}{|U|+2} \right) \right] \\ & \leq \sum_{x_i \in U_0} \min_{x_j \in U} K_p(x_i, x_j) \left(\frac{-1}{|U|(|U|+1)(|U|+2)} \right) \leq 0 \end{aligned}$$

Part 2

$$\begin{aligned} & \sum_{x_i \in U_1} \left(\left(\frac{\min_{x_j \in U} K_p(x_i, x_j)}{|U|+1} - \frac{\min_{x_j \in U} K_p(x_i, x_j)}{|U|} \right) + \left(\frac{K_p(x_i, v_1)}{|U|+1} - \frac{K_p(x_i, v_1)}{|U|+2} \right) \right) \\ & + \left(\frac{\min_{x_j \in U} K_p(x_j, v_1)}{|U|+1} - \frac{\min_{x_j \in U \cup \{v_2\}} K_p(x_j, v_1)}{|U|+2} \right) \\ & = \sum_{x_i \in U_1} \left(-\frac{\min_{x_j \in U} K_p(x_i, x_j)}{|U|(|U|+1)} + \frac{K_p(x_i, v_1)}{(|U|+1)(|U|+2)} \right) + \frac{\min_{x_j \in U} K_p(x_j, v_1)}{(|U|+1)(|U|+2)} \\ & \leq \sum_{x_i \in U_1} \left(-\frac{K_p(x_i, v_1) + 1}{|U|(|U|+1)} + \frac{K_p(x_i, v_1)}{(|U|+1)(|U|+2)} \right) + \frac{\min_{x_j \in U} K_p(x_j, v_1)}{(|U|+1)(|U|+2)} \\ & = \frac{1}{|U|(|U|+1)(|U|+2)} \left(-2 \sum_{x_j \in U_1} K_p(x_i, v_1) + |U| \min_{x_j \in U} K_p(x_j, v_1) - |U_1|(|U|+2) \right) \\ & \leq \frac{1}{|U|(|U|+1)(|U|+2)} \left(-2|U_1| \min_{x_j \in U} K_p(x_j, v_1) + |U| \min_{x_j \in U} K_p(x_j, v_1) - |U_1|(|U|+2) \right) \\ & \leq \frac{1}{|U|(|U|+1)(|U|+2)} (-2|U_1|^2 - 2|U_1|) \leq 0 \end{aligned}$$

Part 3

$$\begin{aligned} & \sum_{x_i \in U_2} \left(\left(\frac{\min_{x_j \in U} K_p(x_i, x_j)}{|U|+1} - \frac{\min_{x_j \in U} K_p(x_i, x_j)}{|U|} \right) + \left(\frac{K_p(x_i, v_2)}{|U|+1} - \frac{K_p(x_i, v_2)}{|U|+2} \right) \right) \\ & + \left(\frac{\min_{x_j \in U} K_p(x_j, v_2)}{|U|+1} - \frac{\min_{x_j \in U \cup \{v_1\}} K_p(x_j, v_2)}{|U|+2} \right) \\ & = \sum_{x_i \in U_2} \left(-\frac{\min_{x_j \in U} K_p(x_i, x_j)}{|U|(|U|+1)} + \frac{K_p(x_i, v_2)}{(|U|+1)(|U|+2)} \right) + \frac{\min_{x_j \in U} K_p(x_j, v_2)}{(|U|+1)(|U|+2)} \\ & \leq \sum_{x_i \in U_2} \left(-\frac{K_p(x_i, v_2) + 1}{|U|(|U|+1)} + \frac{K_p(x_i, v_2)}{(|U|+1)(|U|+2)} \right) + \frac{\min_{x_j \in U} K_p(x_j, v_2)}{(|U|+1)(|U|+2)} \\ & = \frac{1}{|U|(|U|+1)(|U|+2)} \left(-2 \sum_{x_j \in U_2} K_p(x_i, v_2) + |U| \min_{x_j \in U} K_p(x_j, v_2) - |U_2|(|U|+2) \right) \\ & \leq \frac{1}{|U|(|U|+1)(|U|+2)} \left(-2|U_2| \min_{x_j \in U} K_p(x_j, v_2) + |U| \min_{x_j \in U} K_p(x_j, v_2) - |U_2|(|U|+2) \right) \\ & \leq \frac{1}{|U|(|U|+1)(|U|+2)} (-2|U_2|^2 - 2|U_2|) \leq 0 \end{aligned}$$

The gain consists of three parts, each of which is non-positive. Therefore, the overall gain is non-positive, and the supermodular property is thus proven. \square

Algorithm 1 PUPO Training

Input: number of epochs E , steps per epoch M , batch size B , scale of training instances N , discount factor γ , learning rate δ
 Init $\theta, \theta^{BL} \leftarrow \theta$
for epoch = 1, ..., E **do**
 for step = 1, ..., M **do**
 $\forall i \in \{1, 2, \dots, B\}$
 $s_i \leftarrow \text{RandomInstance}()$
 $\tau^i \leftarrow \text{SampleRollout}(s_i, p_\theta)$
 $\tau^{i,BL} \leftarrow \text{GreedyRollout}(s_i, p_{\theta^{BL}})$
 $U_0^i \leftarrow s_i$
 for time = 1, ..., $N - 1$ **do**
 $U_t^i \leftarrow U_{t-1}^i \setminus \tau_t^i$
 $\phi(U_t^i) \leftarrow \sum_{\substack{a \in U_t^i \\ b \in U_t^i \\ b \neq a}} \min K_p(a, b, s_i)$
 $C(U_t^i, \tau_{t+1}^i) \leftarrow K_p(\tau_t^i, \tau_{t+1}^i, s_i) + \frac{\phi(U_{t+1}^i)}{|U_{t+1}^i|} - \frac{\phi(U_t^i)}{|U_t^i|}$
 $W_{t+1}^i \leftarrow 1 + \sum_{j=t}^N \gamma^{j-t} C(U_j^i, \tau_{j+1}^i)$
 end for
 $\nabla \hat{\mathcal{L}} \leftarrow \frac{1}{B} \sum_{i=1}^B (L(\tau^i) - L(\tau^{i,BL})) \cdot \left(\sum_{t=2}^N W_t^i \nabla_\theta \log p_\theta(\tau_t^i | \tau_{1:t-1}^i, s_i) \right)$
 $\theta \leftarrow \theta + \delta \nabla \hat{\mathcal{L}}$
 end for
 $\theta^{BL} \leftarrow \text{UpdateBaseline}(\theta, \theta^{BL})$
 end for

F. The Whole PUPO Algorithm

The whole algorithm of PUPO is presented in Algorithm 1. PUPO is established upon the REINFORCE with baseline, incorporating PuLa information into the modified policy gradient. At different stages of solution construction, PUPO introduces discounted cost information that reflects the purity potential of the partial solution and the unvisited vertex set, which encourages the model to take actions with lower purity orders at each step during the training process. This approach helps the model to learn consistent patterns with the PuLa prior, an information that is independent of specific instances, thereby enhancing its generalization ability. Notably, PUPO can be easily integrated with arbitrary existing constructive neural solvers, without any alterations to network architecture.

G. Detailed Experimental Result

Table 8 shows the training time per epoch with different methods. We can see that the training time of PUPO does not increase significantly owing to the tensorizable computation. The experimental results of the specific tour length is presented in Table 9. Table 10 illustrates the solving time of Vanilla-trained and PUPO-trained models on randomly generated dataset. Following the table, it can be observed that there is almost no difference between Vanilla and PUPO. The numerical results of purity metrics for all models are presented in Table 11. Following the table, PUPO-trained models possess the ability to generate solutions with more outstanding purity.

Table 8. The numerical results of training time (min) per epoch during different training.

	AM-50	AM-100	INViT-50	INViT-100
Vanilla	3.05	4.49	7.72	15.75
PUPO	5.95	14.20	11.598	21.40

Table 9. The length of tours generated from each model after different training on randomly generated dataset.

		AM-50		AM-100		PF-50		PF-100		INVit-50		INVit-100	
		Vanilla	PUPO	Vanilla	PUPO	Vanilla	PUPO	Vanilla	PUPO	Vanilla	PUPO	Vanilla	PUPO
Uniform	100	8.28	8.29	8.27	8.23	8.19	8.21	8.15	8.13	8.03	8.04	8.07	8.05
	1000	31.47	31.12	30.47	30.22	32.74	32.30	30.32	30.17	24.91	24.88	24.94	24.67
	5000	85.75	84.28	92.20	85.97	109.00	104.18	92.18	90.62	55.85	55.69	55.84	55.15
	10000	-	-	-	-	-	-	-	-	79.07	78.88	78.79	77.87
Clustered	100	5.72	5.73	5.71	5.63	5.71	5.71	5.68	5.67	5.46	5.46	5.50	5.48
	1000	19.82	19.65	19.39	18.80	21.26	21.05	20.78	20.30	15.25	15.19	15.24	15.07
	5000	53.06	52.50	52.64	50.77	70.86	69.10	70.71	66.13	32.79	32.66	32.73	32.39
	10000	-	-	-	-	-	-	-	-	44.88	44.58	44.72	44.17
Explosion	100	6.86	6.87	6.86	6.83	6.86	6.87	6.84	6.83	6.67	6.66	6.70	6.68
	1000	21.90	21.84	21.47	21.03	23.50	23.36	22.72	22.10	17.67	17.60	17.67	17.53
	5000	57.30	55.81	58.14	55.62	77.35	75.30	72.57	69.02	37.52	37.28	37.23	36.88
	10000	-	-	-	-	-	-	-	-	43.28	43.05	43.18	42.66
Implosion	100	7.48	7.49	7.48	7.45	7.45	7.47	7.43	7.42	7.29	7.29	7.32	7.30
	1000	27.61	27.57	26.63	26.33	29.39	29.04	27.28	26.95	21.64	21.63	21.69	21.51
	5000	72.59	71.24	71.28	68.46	100.18	95.14	86.94	80.27	44.96	44.83	45.05	44.78
	10000	-	-	-	-	-	-	-	-	72.24	71.79	72.17	71.18

Table 10. The solving time for each model with different training methods on randomly generated dataset.

		AM-50		AM-100		PF-50		PF-100		INVit-50		INVit-100	
		Vanilla	PUPO	Vanilla	PUPO	Vanilla	PUPO	Vanilla	PUPO	Vanilla	PUPO	Vanilla	PUPO
Uniform-100		0.20	0.22	0.21	0.22	2.02	1.97	1.00	1.02	0.85	0.80	1.07	0.91
Uniform-1000		2.35	2.34	2.41	2.40	23.67	24.08	13.57	14.18	13.24	12.88	17.83	17.34
Uniform-5000		19.68	19.10	20.00	19.57	246.65	246.12	205.14	204.15	91.20	89.44	120.07	119.87
Uniform-10000		-	-	-	-	-	-	-	-	224.99	223.69	288.44	287.11
Cluster-100		0.21	0.21	0.21	0.21	2.08	2.13	0.97	0.98	0.84	0.80	1.04	1.17
Cluster-1000		2.35	2.35	2.44	2.43	25.28	26.11	14.05	15.28	13.00	12.77	17.57	16.56
Cluster-5000		19.16	19.38	19.99	19.35	275.68	274.49	212.36	211.68	89.48	88.23	118.63	117.31
Cluster-10000		-	-	-	-	-	-	-	-	222.47	222.32	288.67	288.90
Explosion-100		0.21	0.21	0.20	0.22	2.18	2.17	0.97	1.09	0.82	0.83	1.05	0.94
Explosion-1000		2.38	2.36	2.46	2.40	25.44	24.53	13.94	13.82	12.94	13.05	17.70	17.98
Explosion-5000		19.30	18.67	19.98	19.57	411.08	411.22	213.01	212.39	89.58	89.93	118.93	118.34
Explosion-10000		-	-	-	-	-	-	-	-	223.24	223.03	288.86	288.32
Implosion-100		0.21	0.20	0.21	0.21	3.02	2.89	1.00	0.97	0.83	0.79	1.05	1.01
Implosion-1000		2.37	2.45	2.45	2.45	20.84	21.01	14.08	13.99	12.91	12.73	17.60	17.31
Implosion-5000		19.95	19.28	19.84	19.30	445.75	444.87	186.14	186.05	89.92	88.30	118.87	118.69
Implosion-10000		-	-	-	-	-	-	-	-	222.56	221.72	289.39	290.99

Purity Law for Generalizable Neural TSP Solvers

Table 11. The numerical results of purity evaluation for each model after different training.

	AM-50						AM-100					
	Prop-0 (%)	Vanilla APO (all)	APO (non-0)	Prop-0 (%)	PUPU APO (all)	APO (non-0)	Prop-0 (%)	Vanilla APO (all)	APO (non-0)	Prop-0 (%)	PUPU APO (all)	APO (non-0)
Uniform-100	75.65%	0.15	1.11	75.29%	0.15	1.11	76.81%	0.15	1.12	79.48%	0.14	1.17
Uniform-1000	62.51%	0.64	1.98	64.32%	0.62	1.92	65.67%	0.52	1.75	67.70%	0.52	1.76
Uniform-5000	24.91%	1.36	2.97	26.39%	1.33	3.05	24.54%	1.50	3.03	26.64%	1.23	2.74
Uniform-10000	-	-	-	-	-	-	-	-	-	-	-	-
Cluster-100	70.66%	0.23	1.26	70.13%	0.24	1.28	72.34%	0.24	1.30	75.35%	0.20	1.28
Cluster-1000	59.13%	0.85	2.30	58.29%	0.80	2.19	61.18%	0.77	2.17	62.52%	0.66	1.97
Cluster-5000	23.65%	1.93	3.88	23%	1.64	3.33	23.58%	1.64	3.31	24.76%	1.48	3.05
Cluster-10000	-	-	-	-	-	-	-	-	-	-	-	-
Explosion-100	73.72%	0.17	1.15	74.35%	0.17	1.14	75.24%	0.17	1.17	77.77%	0.17	1.22
Explosion-1000	62.92%	0.69	2.03	61.35%	0.67	2.03	63.32%	0.62	1.89	65.58%	0.57	1.84
Explosion-5000	25.09%	1.53	3.27	23.99%	1.41	3.06	24.20%	1.55	3.13	26.04%	1.30	2.82
Explosion-10000	-	-	-	-	-	-	-	-	-	-	-	-
Implosion-100	72.97%	0.19	1.20	73.50%	0.19	1.19	74.80%	0.19	1.23	77.27%	0.18	1.26
Implosion-1000	61.52%	0.77	2.22	60.27%	0.77	2.20	64.14%	0.65	2.01	65.01%	0.62	1.95
Implosion-5000	24.05%	1.93	3.83	23.70%	1.69	3.41	24.12%	1.65	3.33	25.30%	1.46	3.07
Implosion-10000	-	-	-	-	-	-	-	-	-	-	-	-
	PF-50						PF-100					
	Prop-0 (%)	Vanilla APO (all)	APO (non-0)	Prop-0 (%)	PUPU APO (all)	APO (non-0)	Prop-0 (%)	Vanilla APO (all)	APO (non-0)	Prop-0 (%)	PUPU APO (all)	APO (non-0)
Uniform-100	77.46%	0.14	1.09	77.57%	0.15	1.10	80.07%	0.12	1.08	80.31%	0.12	1.08
Uniform-1000	59.68%	0.74	2.00	60.73%	0.70	1.94	65.66%	0.56	1.78	66.06%	0.54	1.75
Uniform-5000	18.66%	2.36	3.92	20.04%	2.14	3.65	23.09%	1.56	2.94	23.60%	1.49	2.92
Uniform-10000	-	-	-	-	-	-	-	-	-	-	-	-
Cluster-100	71.41%	0.24	1.27	71.53%	0.25	1.29	72.49%	0.24	1.29	73.64%	0.23	1.28
Cluster-1000	52.39%	1.21	2.67	52.53%	1.17	2.60	54.38%	1.09	2.54	56.51%	0.97	2.37
Cluster-5000	15.08%	4.52	6.54	15.42%	4.06	5.95	16.08%	4.20	6.31	18%	3.13	4.93
Cluster-10000	-	-	-	-	-	-	-	-	-	-	-	-
Explosion-100	74.92%	0.19	1.16	74.82%	0.18	1.17	76.63%	0.17	1.17	77.34%	0.16	1.16
Explosion-1000	55.35%	0.98	2.33	55.95%	0.98	2.34	57.53%	0.89	2.21	59.66%	0.81	2.12
Explosion-5000	16.05%	3.52	5.18	16.64%	3.39	5.10	17.60%	3.01	4.62	18.77%	2.73	4.40
Explosion-10000	-	-	-	-	-	-	-	-	-	-	-	-
Implosion-100	73.76%	0.24	1.30	73.68%	0.24	1.28	75.67%	0.22	1.29	76.24%	0.22	1.29
Implosion-1000	54.17%	1.40	3.09	55.04%	1.42	3.15	59.29%	1.14	2.79	60.07%	1.13	2.81
Implosion-5000	15.18%	8.14	10.81	15.90%	8.46	11.59	17.79%	7.46	10.38	18.88%	6.02	8.88
Implosion-10000	-	-	-	-	-	-	-	-	-	-	-	-
	INVt-50						INVt-100					
	Prop-0 (%)	Vanilla APO (all)	APO (non-0)	Prop-0 (%)	PUPU APO (all)	APO (non-0)	Prop-0 (%)	Vanilla APO (all)	APO (non-0)	Prop-0 (%)	PUPU APO (all)	APO (non-0)
Uniform-100	81.52%	0.10	1.05	0.82	0.10	1.04	80.95%	0.11	1.07	0.82	0.10	1.05
Uniform-1000	86%	0.16	1.37	0.86	0.15	1.33	85.80%	0.17	1.43	0.87	0.14	1.33
Uniform-5000	43.52%	0.18	1.56	0.44	0.17	1.05	43.38%	0.20	1.61	0.44	0.17	1.48
Uniform-10000	87.39%	0.18	1.55	0.88	0.17	1.50	87.32%	0.20	1.65	0.88	0.16	1.47
Cluster-100	79.78%	0.14	1.18	0.80	0.13	1.17	79.26%	0.16	1.26	0.80	0.14	1.19
Cluster-1000	86.02%	0.22	1.88	0.86	0.19	1.63	85.56%	0.23	1.83	0.87	0.18	1.61
Cluster-5000	43.72%	0.20	1.61	0.44	0.18	1.55	43.32%	0.27	2.20	0.44	0.17	1.52
Cluster-10000	87.40%	0.84	6.91	0.88	0.88	7.34	87.15%	0.71	5.74	0.88	0.87	7.77
Explosion-100	80.56%	0.12	1.11	0.81	0.12	1.11	80.09%	0.13	1.15	0.81	0.12	1.11
Explosion-1000	85.42%	0.30	2.34	0.86	0.28	2.23	85.09%	0.30	2.33	0.86	0.26	2.16
Explosion-5000	43.54%	0.42	3.47	0.44	0.48	4.07	43.40%	0.53	4.33	0.44	0.43	3.73
Explosion-10000	87%	0.95	7.68	0.87	1.03	8.38	87%	0.97	7.58	0.88	0.88	7.57
Implosion-100	79.98%	0.12	1.12	0.80	0.12	1.12	79.77%	0.14	1.17	0.80	0.13	1.13
Implosion-1000	85.69%	0.19	1.54	0.86	0.18	1.54	85.39%	0.21	1.64	0.86	0.18	1.55
Implosion-5000	43.39%	0.23	1.88	0.44	0.22	1.81	43.33%	0.24	1.92	0.44	0.19	1.66
Implosion-10000	87.34%	0.30	2.47	0.88	0.29	2.39	87.16%	0.27	2.18	0.88	0.30	2.62